Decay of polar cap patch

K. Hosokawa,[1,2] J. I. Moen,[1] K. Shiokawa,[3] and Y. Otsuka[3]

Received 17 November 2010; revised 19 January 2011; accepted 17 February 2011; published 10 May 2011.

[1] We report an event in which a polar cap patch was detected with an all-sky imager (ASI) at Resolute Bay, Canada (74.73° N, 265.07° E; AACGM latitude 82.9°), on the nightside. The patch stopped its antisunward motion associated with a northward turning of interplanetary magnetic field and stayed within the field of view of the ASI for more than 1 h. When the patch stagnated, its luminosity decreased gradually, which allows us to investigate how the patch plasma decayed in a quantitative manner. The decay of the patch can be quantitatively explained by the loss through recombinations of O^+ with ambient N_2 and O_2 molecules, if we assume the altitude of the optical patch to be around 295 km. The derived altitude of the patch around 295 km is much higher than the nominal value at 235 km obtained from the MSIS-E90 and IRI-2007 models, indicating that climatological models such as IRI are not suitable for describing the actual density profile of patches. This is probably because the loss process was much faster in the lower-altitude part of the patch; thus, the peak altitude of the patch increased as it traveled across the polar cap because of rapid recombination at the bottomside of the *F* region. This suggests that we should employ higher emission altitude when we investigate optical patches transported deep into the nightside polar cap. Such information is important when we compare the optical data with other instruments such as coherent radars and GPS scintillation measurements by mapping the all-sky image on the geographic coordinate system with an assumption of the patch emission altitude.

Citation: Hosokawa, K., J. I. Moen, K. Shiokawa, and Y. Otsuka (2011), Decay of polar cap patch, *J. Geophys. Res.*, *116*, A05306, doi:10.1029/2010JA016297.

1. Introduction

[2] Polar cap patches, regions of high-density plasma often appearing in the polar cap *F* region ionosphere, are thought to be generated near the cusp when the interplanetary magnetic field (IMF) is directed predominantly southward [*Crowley*, 1996, and references therein]. The horizontal extent of patches typically ranges from 100 km to 1000 km [*Coley and Heelis*, 1995], and the plasma density within them is often enhanced by a factor of 2–10 above that in the surrounding region [*Weber et al.*, 1984]. The dynamical properties of patches have been investigated by using all-sky airglow imager [*Weber et al.*, 1984; *Hosokawa et al.*, 2006; *Moen et al.*, 2007], coherent HF radar [*Milan et al.*, 2002; *Hosokawa et al.*, 2009a], incoherent scatter radar [*Pedersen et al.*, 2000], and ionosonde [*MacDougall and Jayachandran*, 2007]. Numerous processes have been proposed to explain the generation of patches, such as the IMF-controlled reorientation of the cusp flow [*Milan et al.*, 2002], convection jets [*Rodger et al.*, 1994], in situ plasma reduction under an intense electric field [*Valladares et al.*, 1994a], expansion of the polar cap convection pattern by pulsed reconnection [*Lockwood and Carlson*, 1992], and bursty plasma transport and patch cutting by FACs at subauroral latitudes [*Moen et al.*, 2006]. Most of the past studies suggested that once the patches are generated on the dayside, they survive for a long time and are transported antisunward over very long distances before they exit the polar cap into the nightside auroral zone. However, it has not been investigated in detail yet how patches decay during their travel through the dark polar cap ionosphere except for the work of *Pedersen et al.* [1998]. *Pedersen et al.* [1998] employed scanning measurements of the Sondrestrom incoherent scatter radar in Greenland to track the large-scale structure of polar cap patches. They observed large-scale latitudinal gradients in average electron density within the field of view (FOV) of the radar, from which they estimated average time constant of the decay of patch plasma to be an order of 1 h. In this paper, we report an event in which a patch, detected as a region of enhanced 630.0 nm airglow emission with an all-sky imager (ASI) in the nightside polar cap, stopped its antisunward motion and stayed within the FOV of the ASI for more than 1 h. When the patch stagnated within the FOV of the ASI, its luminosity decreased very gradually. By investigating the temporal variation of the patch luminosity, we evaluate its loss

[1]Department of Physics, University of Oslo, Oslo, Norway.
[2]Department of Communication Engineering and Informatics, University of Electro-Communications, Tokyo, Japan.
[3]Solar-Terrestrial Environment Laboratory, Nagoya University, Nagoya, Japan.

0148-0227/11/2010JA016297

process in a quantitative manner and discuss the factors controlling the decay of patches.

2. Instrumentation

[3] The ASI employed in this study has been operational at Resolute Bay, Canada (74.73° N, 265.07° E; AACGM latitude 82.9°) since January 2005 [*Hosokawa et al.*, 2006] as part of the Optical Mesosphere Thermosphere Imagers (OMTIs) [*Shiokawa et al.*, 1999, 2009] developed by the Solar-Terrestrial Environment Laboratory, Nagoya University. This imager has a number of optical filters, such as 557.7 nm, 630.0 nm, 777.4 nm, Na line, and OH band; this enables us to study various upper atmospheric phenomena occurring in the polar cap region, such as polar cap patches [*Hosokawa et al.*, 2006, 2009a, 2009b, 2010a], tongue of ionization [*Hosokawa et al.*, 2009c, 2010b], polar cap aurora [*Koustov et al.*, 2008; *Jayachandran et al.*, 2009; *Hosokawa et al.*, 2011], and gravity waves at mesospheric heights [*Suzuki et al.*, 2009]. The airglow intensity at a wavelength of 630.0 nm (O I 6300) obtained using a ground-based imager is known to be proportional to the electron density at 200–300 km altitudes in the *F* region [*Barbier*, 1959; *Barbier and Glaume*, 1962]. In this study, all-sky airglow images at the wavelength of 630.0 nm, which are obtained every 2 min with an exposure time of 30 s, are employed for visualizing the 2-D structure of patches in the polar cap region. One thing we have to keep in mind is that the 630.0 nm emission has a strong relation to the neutral density (O_2 and N_2) and therefore altitude of patches in addition to the dependence on the electron density [e.g., *Makela et al.*, 2001]. For example, *Sojka et al.* [1997] suggested, by using physical model of the ionosphere, that the 630.0 nm emission intensity is linearly related to the *F* region electron density only when the height of the *F* region peak is constant everywhere in the polar cap. Thus, care must be taken when we interpret the behavior of optical patches in the 630.0 nm all-sky images. Background continuum emission from the sky is sampled every 20 min at a wavelength of 572.5 nm and is used to derive the absolute intensity of the airglow lines [*Shiokawa et al.*, 2000, 2009].

3. Observations

[4] The interval presented is a 7 h period from 0400 to 1100 UT on 4 March 2010, during which a patch detected with the ASI stopped its antisunward motion and stagnated within the FOV. Figure 1a shows a 630.0 nm all-sky image taken at 0714 UT, about 20 min before the stagnation. To indicate the slight airglow enhancement caused by patches, the airglow distribution is shown as a percentage deviation from a 1 h running average [*Hosokawa et al.*, 2010a]. At this time, a large patch, which we denote as "patch F" hereafter, can be identified near the zenith. This patch first appeared from the northwestern horizon and drifted southeastward along the SE-NW cross section indicated by the dashed line. Soon after its passage across the zenith, patch F stopped its southeastward motion and stayed within the FOV for more than 1 h. Figure 1b again shows the 630.0 nm optical image taken at 0714 UT in another format. Here, however, the all-sky image is converted into the altitude adjusted corrected geomagnetic (AACGM) coordinates [*Baker and Wing*, 1989] assuming an emission height of 290 km and then mapped into coordinates of magnetic local time (MLT) and magnetic latitude (MLAT). At this time, the center of patch F was located above 80° MLAT near midnight and moving antisunward along the SW-NW cross section. In order to see how patch F stagnated, we present a stripe of pixels from the image sequence in a keogram format along the NW-SE axis. During the first half of the interval, sequence of patches (patches A-E) were observed as slanted bright traces. They appeared from the northwestern edge of the FOV, moved southeastward across the zenith, and eventually got out of the FOV in the southeastern edge of the FOV. Patch F also appeared from the northwestern edge of the FOV at around 0630 UT and drifted southeastward. In contrast to patch A-E, however, patch F stopped its southeastward motion at around 0733 UT, which is indicated by the vertical dashed line. After that, it underwent an oscillation NW-SE-NW within the FOV until it disappeared around 0900 UT. An animation showing the temporal evolution of the patches during a 7 h interval from 0400 UT to 1100 UT at a rate of one frame every 2 min accompanies the online version of this article (Animation S1).[1] The movie better demonstrates how the patch stagnated and decayed subsequently. The Important point is that the optical intensity of patch F decreased during this time period, which allows us to investigate how polar cap patches decay through recombination.

[5] To understand why the cross-polar drift of patch F stopped, we plot the IMF B_z during this interval in Figure 1d. These IMF data were obtained by the Geotail spacecraft located upstream of the Earth (X_{GSM} = 22.7 R_e). A solar wind velocity of approximately 440 km s^{-1} and a proton density of 1.2 cc^{-1} were measured also by Geotail around the stagnation, implying a delay of 12 min between the observed IMF feature at the spacecraft and its incidence on the dayside magnetopause. An additional 2 min were added to account for the propagation of Alfvén waves from the subsolar magnetopause to the dayside polar cap. These calculations were carried out by the technique proposed by *Khan and Cowley* [1999], and successfully applied in timing of the auroral cusp reconfiguration due to an IMF B_y polarity change by *Moen et al.* [1999]. In Figure 1d, the time series of the IMF is shifted accordingly. The IMF B_z was predominantly negative before the stagnation, indicating a favorable condition for the generation of patches near the cusp and subsequent delivery into the polar cap [*Crowley*, 1996]. The patch sequence (A-E) drifting across the FOV was observed during this interval of southward IMF. At around 0720 UT, about 10–15 min before the stagnation of patch F, the IMF turned to northward. After that, the IMF B_z was mostly positive until the end of this interval, which is, in turn, a favorable condition for the formation of polar cap arcs [*Valladares et al.*, 1994b; *Hosokawa et al.*, 2011]. It is interesting to note that there existed the ≈ 10–15 min delay time between the northward turning of the IMF and stagnation in the cross-polar plasma transport. Such a time delay gives some information on the response time of the high-latitude convection to changes of the upstream IMF orientation. *Cowley and Lockwood* [1992] proposed a ≈ 15 min

[1] Auxiliary materials are available in the HTML. doi:10.1029/2010JA016297.

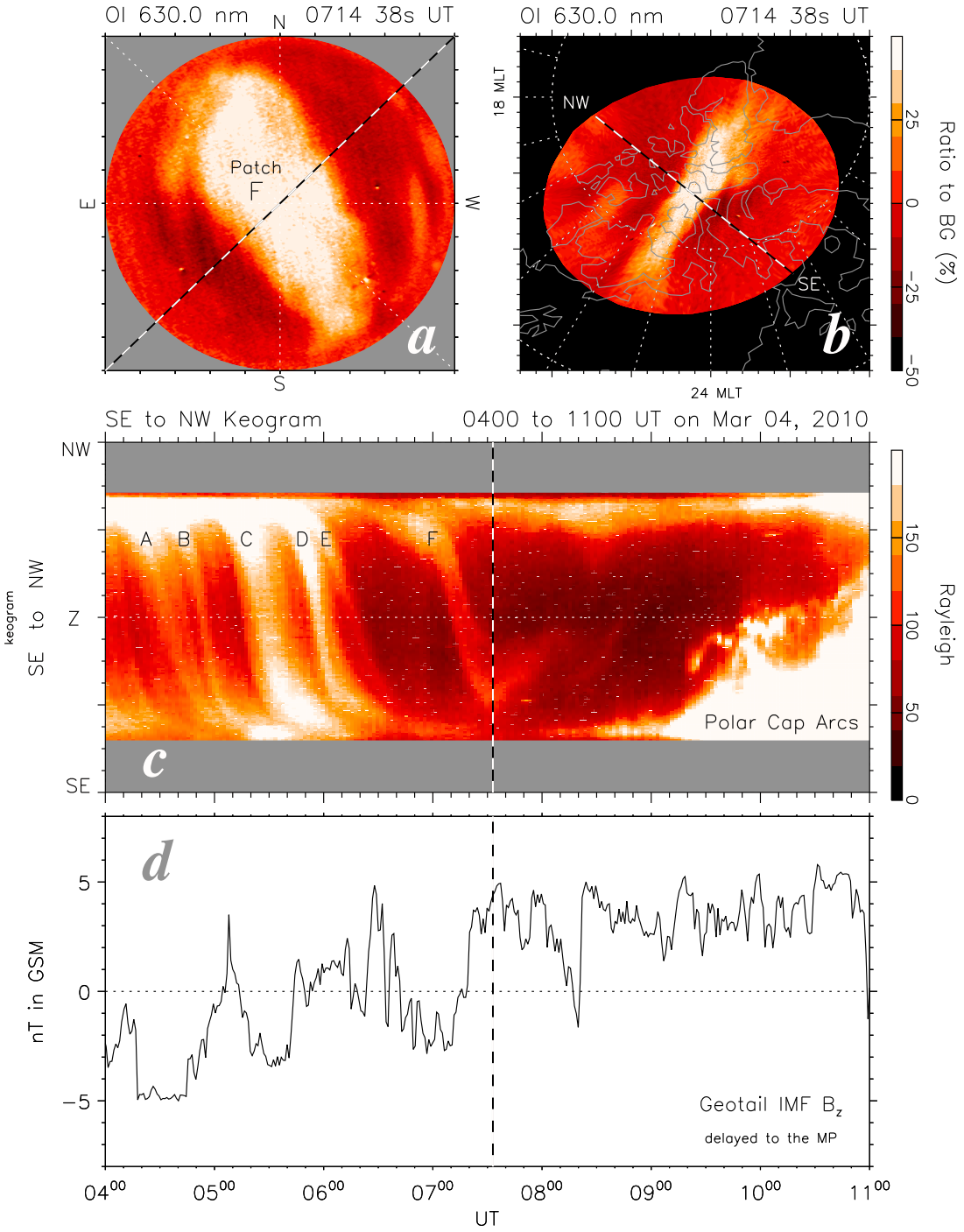

Figure 1. (a) A 630.0 nm all-sky image at 0714 UT on 4 March 2010. To indicate the slight enhancement in the airglow intensity caused by patches, the airglow distribution is shown as a percentage deviation from a 1 h running average. (b) Same data as in Figure 1a, but the raw all-sky image is converted into the AACGM coordinates [*Baker and Wing*, 1989] assuming an emission height of 280 km and is then mapped into coordinates of MLT and MLAT. Magnetic midnight is to the bottom, and the dotted circle represents MLAT of 80°. (c) Keogram reproduced from 630.0 nm all-sky images along the SE-NW cross section shown in Figure 1a. (d) IMF B_z measured by the Geotail spacecraft. The time series is time shifted by 14 min to allow for solar wind propagation delay.

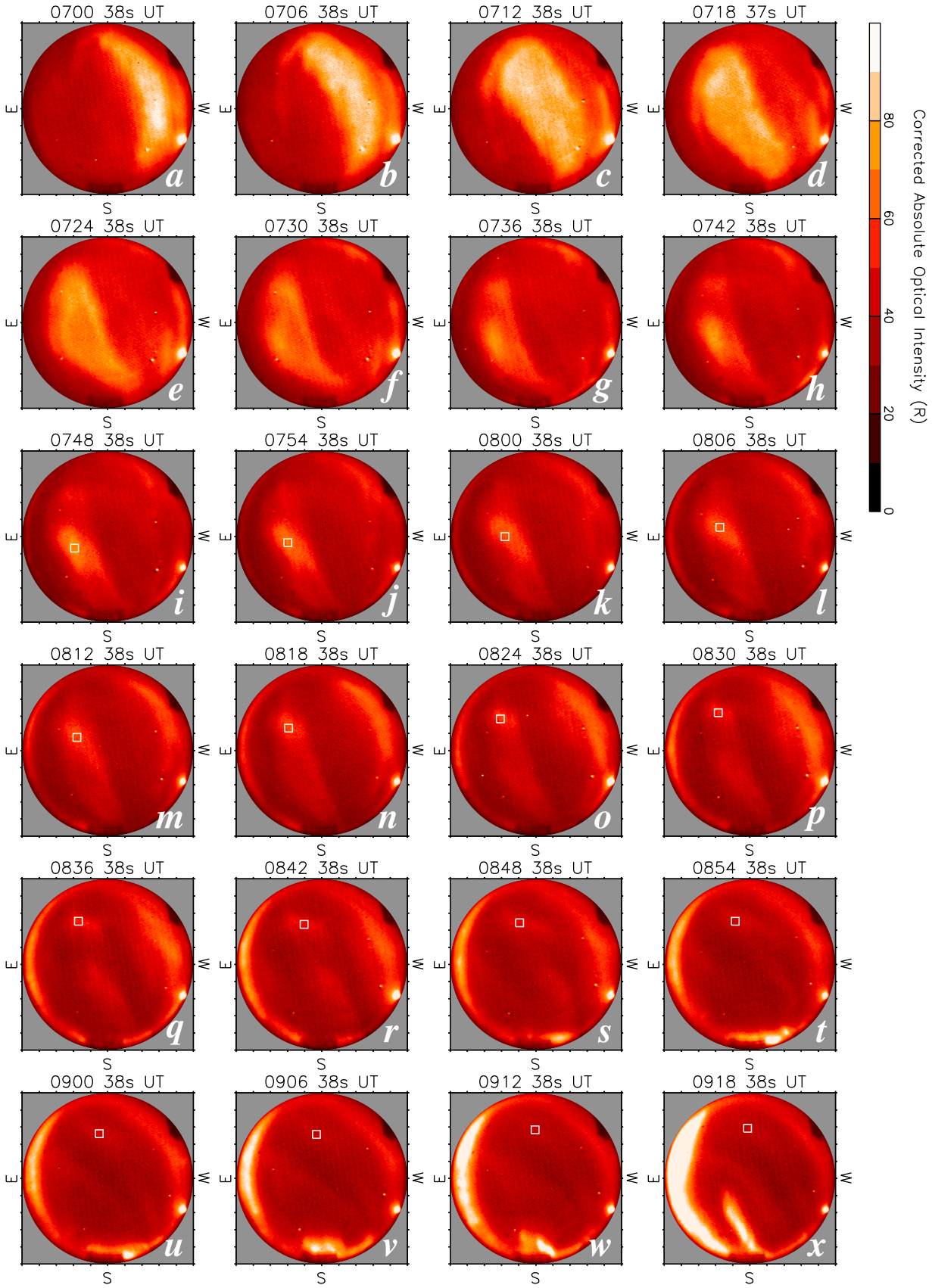

Figure 2. Sequence of 630.0 nm airglow images obtained at 6 min intervals from 0700 to 0918 UT. The effects of the dependence of the optical intensity on the zenith angle are corrected according to the procedure introduced by *Kubota et al.* [2001].

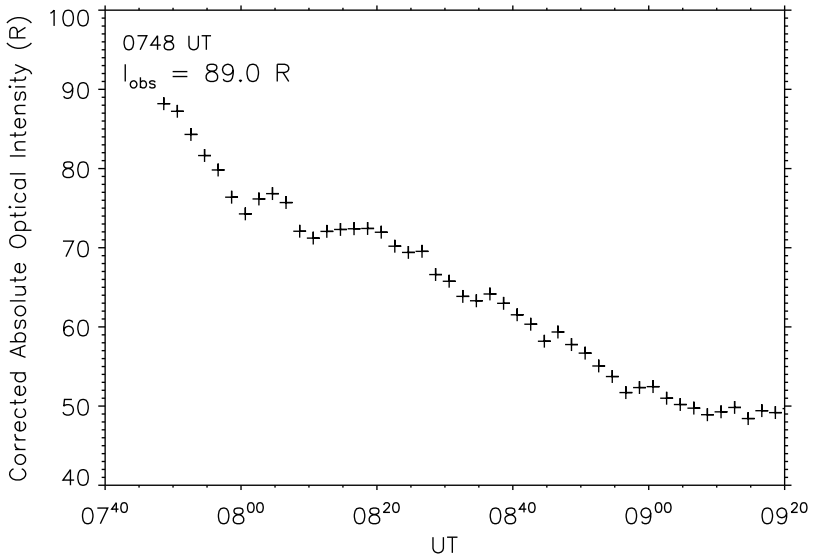

Figure 3. Time series of the 630.0 nm optical intensity at the center of patch F after 0748 UT.

equilibrium time for reconnection-driven excitation of twin-cell flow, of which firm experimental evidence was presented by *Lockwood et al.* [1993] and *Moen et al.* [1995, 1996]. Further evidence was recently given by *Bahcivan et al.* [2010] who employed an incoherent scatter radar data at Resolute Bay to estimate the response of the polar cap convection to the southward turning of the IMF. They investigated 10 events of clear southward turning of the IMF and derived an average response time of 13 min. The delay identified during the current interval is fairly consistent with the value obtained by *Bahcivan et al.* [2010].

[6] Figure 2 shows a sequence of 630.0 nm all-sky airglow images picked at 6 min intervals from 0700 UT to 0918 UT. At 0700 UT (Figure 2a), patch F just appeared from the northwestern part of the FOV. Subsequently, patch F continued drifting southeastward until it stagnated at around 0736 UT (Figure 2g). After that, it wandered around on the northern part of the FOV until it faded below the sensitivity threshold of the ASI. Now we try to extract the temporal variation of the luminosity of patch F from the all-sky images shown in Figure 2. Before moving on, we must note that the patch brightness observed by ASIs depends on the zenith angle. Thus, care must be taken when we extract the temporal variation of the luminosity of a patch moving across the FOV. There are at least three factors affecting the luminosity of patches [*Tohmatsu and Ogawa*, 1990]: (1) sensitivity decrease with increasing zenith angle, (2) the so-called van Rhijn effect (increase in the volume per pixel with increasing zenith angle), and (3) atmospheric extinction. We carefully removed these effects by using the procedure introduced by *Kubota et al.* [2001]. The optical data calibrated through this procedure are displayed in Figure 2. Before 0742 UT (Figure 2h), it is rather difficult to locate the center of patch F, because the region of enhanced luminosity was very broad and it showed some complicated temporal evolution such as a splitting seen in Figures 2f–2h. Such a splitting may be caused by a shear in the background convection as suggested by *Hosokawa et al.* [2010a]. Thus, we start sampling the optical intensity at 0748 UT, after which the spatial structure of patch F was relatively stable. In Figures 2i–2x, the optical intensities within the white rectangle near the center of patch F are averaged and plotted in Figure 3 as a time series. It is clearly seen that the time series of the patch luminosity decreased gradually.

4. Discussion and Summary

[7] The 630.0 nm optical emission associated with patches comes from the following chemistry:

$$O_2^+ + e \rightarrow O + O^*. \tag{1}$$

The exited O emits the 630.0 nm emission that is used to monitor polar cap patches with ASIs. According to this equation, the 630.0 nm emission intensity at a certain altitude is proportional to the rate at which O_2^+ recombines, i.e.,

$$I_{630.0nm} = A\alpha\left[O_2^+\right][O^+], \tag{2}$$

where A is some positive constant, and α is the recombination rate for O_2^+, which is in principle a function of the electron temperature and is assumed here to be constant in time. In this expression, we assume that the electron density is equal to $[O^+]$, which is a very good approximation in the F region. This equation may give an impression that the 630.0 nm emission intensity is independent of the neutral density. However, the emission intensity highly depends on the density of N_2 and O_2 [e.g., *Makela et al.*, 2001], which will be described in greater detail later. The density of O^+ in this equation can be determined by the following continuity equation:

$$\frac{D[O^+]}{Dt} = P - L - [O^+]\nabla \cdot \mathbf{v}, \tag{3}$$

where $D/Dt = \partial/\partial t + \mathbf{v} \cdot \nabla$ is the convective derivative, P and L are the chemical production and loss rates, respec-

tively, and **v** is the ion drift. This equation describes the temporal variation of $[O^+]$ in a reference frame moving with a patch that is transported by the background convection. We are dealing here with a situation for which there is no sunlight and no particle precipitation; thus, $P \approx 0$. For simplicity, we ignore the density variation associated with the divergence in the ion drift ($[O^+] \nabla \cdot \mathbf{v}$). Hence, $[O^+]$ is controlled only by the loss term (L) through the following reactions:

$$O^+ + N_2 \rightarrow NO^+ + O \tag{4}$$

$$O^+ + O_2 \rightarrow O_2^+ + O. \tag{5}$$

Using k_1 and k_2 for the reaction rates associated with reactions (4) and (5), we obtain

$$\frac{D[O^+]}{Dt} = -(k_1[N_2] + k_2[O_2])[O^+]. \tag{6}$$

Then, $[O^+]$ will decay in time as

$$[O^+] = [O^+]_0 \exp(-\beta t), \tag{7}$$

where $[O^+]_0$ is the density of O^+ at $t = 0$, and $\beta = k_1\,[N_2] + k_2\,[O_2]$ is a loss rate. The density of O_2^+ in equation (2) is given by equating production through reaction (5) with loss through reaction (1) for that ion:

$$\alpha[O_2^+][O^+] = k_2[O^+][O_2]. \tag{8}$$

Here, we again assume that the electron density is equal to $[O^+]$ in the F region. By using equations (7) and (8), we can rewrite equation (2) and obtain

$$I_{630.0nm} = B \exp(-\beta t), \tag{9}$$

where $B = Ak_2\,[O_2][O^+]_0$. If we assume that k_2 and $[O_2]$ do not change very much during the stagnation of patch F, B can be treated as constant in time. In such a case, B gives the optical intensity at $t = 0$ and the patch luminosity decays exponentially with an e-folding time of β^{-1}.

[8] Hereafter, we try to explain the decay of the patch luminosity shown in Figure 3 through the loss process described above. Important thing to bear in mind is that equation (9) gives the optical intensity at a certain height h; thus, B and β in the equation are functions of altitude. In order to evaluate the observed column emission I_{obs} more precisely, we have to take the altitude profile of these parameters into account:

$$I_{obs} = \int_{h1}^{h2} I_{630.0nm} dh = \int_{h1}^{h2} B(h) \exp(-\beta(h)t) dh, \tag{10}$$

where h_1 and h_2 is the lower and upper boundary of the 630.0 nm emission layer, respectively. First, we estimate how $\beta(h)$ changes with altitude by using empirical expressions for k_1 and k_2, and the density of molecules obtained from a model. The reaction rates k_1 and k_2 for reactions (4) and (5) (in units of $m^3\ s^{-1}$) are obtained by the following equation derived by *McFarland et al.* [1973]:

$$k_1 = 8.0 \times 10^{-20} \left(\frac{T_{eff}}{300}\right)^{2.0} \tag{11}$$

$$k_2 = 2.0 \times 10^{-17} \left(\frac{300}{T_{eff}}\right)^{0.4}, \tag{12}$$

where T_{eff} is the effective temperature in K. The expression for the effective temperature is known to take a simple form at altitudes above about 200 km [*Schunk et al.*, 1975]:

$$T_{eff} = T_n + 0.329\ E_\perp^2. \tag{13}$$

In this expression, T_n is the neutral temperature in K and $E_\perp$ is the effective electric field in mV m^{-1} measured in the moving frame of the neutral gas. As shown in section 3, patch F nearly stopped its motion at around 0733 UT; thus, the magnetospheric electric field forcing can be neglected. However, this does not allow us to ignore the effective electric field in equation (13) because neutral particles were still in motion after the patch got stagnated. Figure 4a shows the altitude profile of the effective temperature calculated by equation (13) using T_n obtain from the MSIS-E-90 model [*Hedin*, 1991]. Here, we employ the effective electric field of 0, 10, and 25 mV m^{-1} for evaluating the impact of the effective electric field on the effective temperature. If larger effective electric field is used, the effective temperature becomes higher due to more frequent collisions between ions and neutrals. Figure 4b shows the altitude profiles of k_1 and k_2 estimated by using equations (11) and (12), respectively. The reaction rates are rather constant for altitudes considered because the effective temperature does not change very much in altitude. Figure 4c shows the densities of N_2 and O_2 obtained again from the MSIS model, both of which decrease very rapidly with increasing altitude. By using the values shown in Figures 4b and 4c, we can estimate the altitude profile of the loss rate $\beta = k_1\,[N_2] + k_2\,[O_2]$. The altitude profile of β is shown in Figure 4d. The loss rate decreases very steeply as the altitude increases, which is mainly because the densities of N_2 and O_2 decrease with increasing altitude. Such a change of β with altitude will introduce different decay rate at different altitude. Another important point is that the change of the effective electric field does not affect β very much. Thus, we assume that the effective temperature is equal to T_n in the following discussion and employ the profile shown by the blue curve in Figure 4d as $\beta\ (h)$ in equation (10). One thing we have to bear in mind is that the above mentioned deviation of $\beta\ (h)$ is largely dependent on unmeasured parameters such as $E_\perp$, T_n, and profiles of N_2 and O_2. We ignore $E_\perp$ and use the MSIS model to generate T_n, and profiles of N_2 and O_2. Such a way of choosing these parameters may affect the results of the current modeling.

[9] In order to model the observed patch luminosity change using equation (10), we also need to estimate the altitude profile of $B(h) = Ak_2\,[O_2][O^+]_0$, which is the optical intensity at a certain height h at $t = 0$. A is a some positive constant independent on altitude and the altitude profiles of

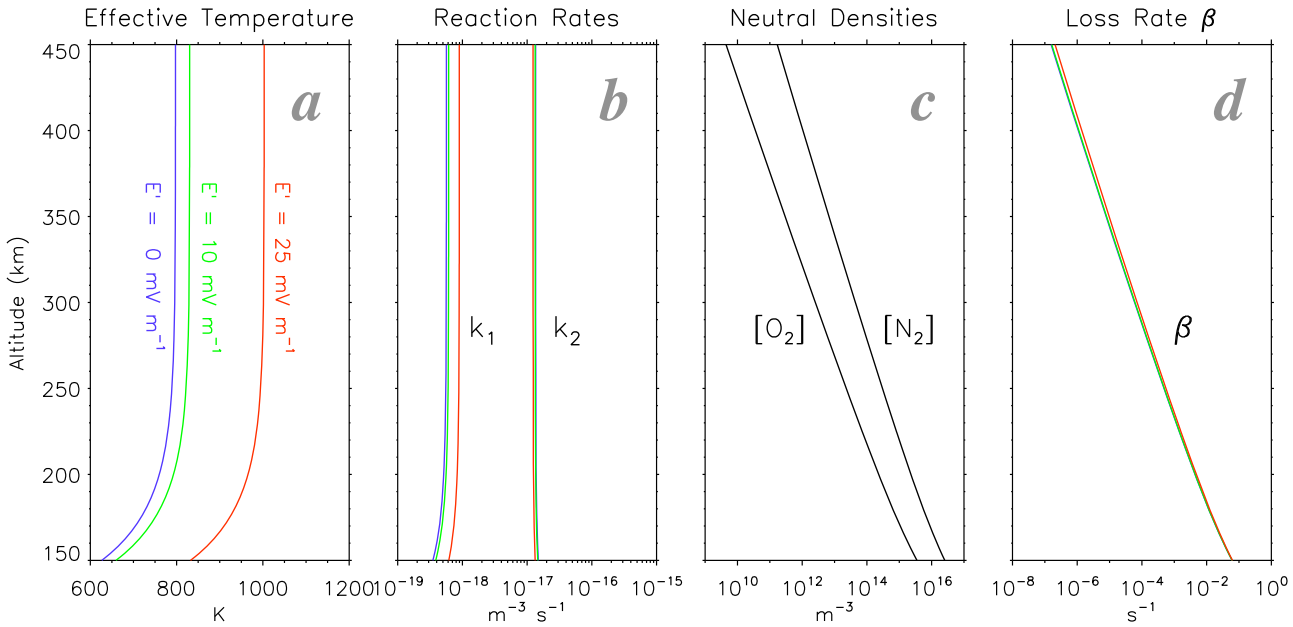

Figure 4. (a) Altitude profile of the effective temperature for three different cases of the effective electric field (0, 10, and 25 mV m^{-1}). (b) Altitude profile of the reaction rates (k_1 and k_2) for reactions (4) and (5) in the text. (c) Altitude profile of the density of N_2 and O_2 taken from the MSIS model. (d) Altitude profile of the loss rate β calculated from the values shown in Figures 4b and 4c.

k_2 and $[O_2]$ can be obtained from the model as shown in Figures 4b and 4c, respectively; thus, $B(h)$ can be calculated if we know the altitude profile of $[O^+]_0$, which is the density of O^+ at $t = 0$. Most reliable way to estimate the altitude profile of $[O^+]_0$ is to employ collaborating measurements of an incoherent scatter radar. During the interval of interest, however, there were no available data from the Resolute Bay incoherent scatter radar (RISR) [*Bahcivan et al.*, 2010]. Thus, instead, we employ the IRI-2007 model [*Bilitza and Reinisch*, 2008] to generate the altitude profile of O^+ although the density profile from IRI cannot be expected to be correct under the circumstances as suggested by *Moen et al.* [2008]. Figure 5a shows the altitude profile of O^+ density obtained from the IRI-2007 model at 0748 UT ($t = 0$) over Resolute Bay, together with the electron density from IRI, $[O_2]$ and $[N_2]$ from MSIS. The profiles of $[O^+]$ and the electron density have a peak at 305 km in altitude, below which the density decreases with decreasing altitude. Figure 5c shows the corresponding altitude profile of the optical intensity $B(h) = Ak_2\,[O_2][O^+]_0$, in which the derived emission intensity is self-normalized. The peak of the emission layer was located around 235 km in altitude, which is slightly lower than the typical values (250–300 km). Using equation (10) with the altitude profiles of β in Figure 4d and $B(h)$ in Figure 5c, we can reproduce the temporal evolution of the emission layer. Figure 5e shows how the altitude profile of the emission intensity changed after 0748 UT ($t = 0$). The optical intensity decreased very rapidly in the first 20 min while the peak of the emission layer increased from 235 km to 260 km. After that the decrease of the emission intensity and the increase of the peak height became more gradual. The red curve in Figure 5g indicates the column optical intensity derived using equation (10), in which we use h_1 and h_2 of 150 km and 450 km, respectively. Also shown for comparison is the time series of the observed patch luminosity introduced in Figure 3. The calculated patch luminosity based on the IRI electron density profile decays much more rapidly in comparison with the observed decay. Hence, the reaction rates are too large, which indicates that the altitude of the emission layer estimated from the IRI model is too low. This suggests that the actual electron density profile ($[O^+]$ profile) had a peak at higher altitude. However, without any knowledge on the actual density profile such as that obtained from an incoherent scatter radar, we cannot definitely determine if the above mentioned discrepancy is primarily caused by the wrong assumption of the emission altitude. Unfortunately, the Resolute Bay incoherent scatter radar (RISR) [*Bahcivan et al.*, 2010] was not operative during the interval of interest. Instead, we try to estimate the peak altitude of the F region from comparison between 630.0 nm and 777.4 nm emissions from the same imager by following the procedure of *Makela et al.* [2001]. Figure 6 (top) shows the time series of the 630.0 nm (blue) and 777.4 nm (red) emissions at the zenith between 0400 and 0900 UT. Note that 777.4 nm emission was sampled only every 20 min. The time series of the 630.0 nm emission shows several peaks associated with the sequential passage of the patches across the zenith. The peak at 0714 UT corresponds to the passage of patch F. *Makela et al.* [2001] demonstrated that h_mF_2 in km can be expressed by the following equation:

$$h_mF_2 = \exp\left(0.171 \times \ln\left(\sqrt{I_{777.4}}/I_{630.0}\right) + 6.43\right). \qquad (14)$$

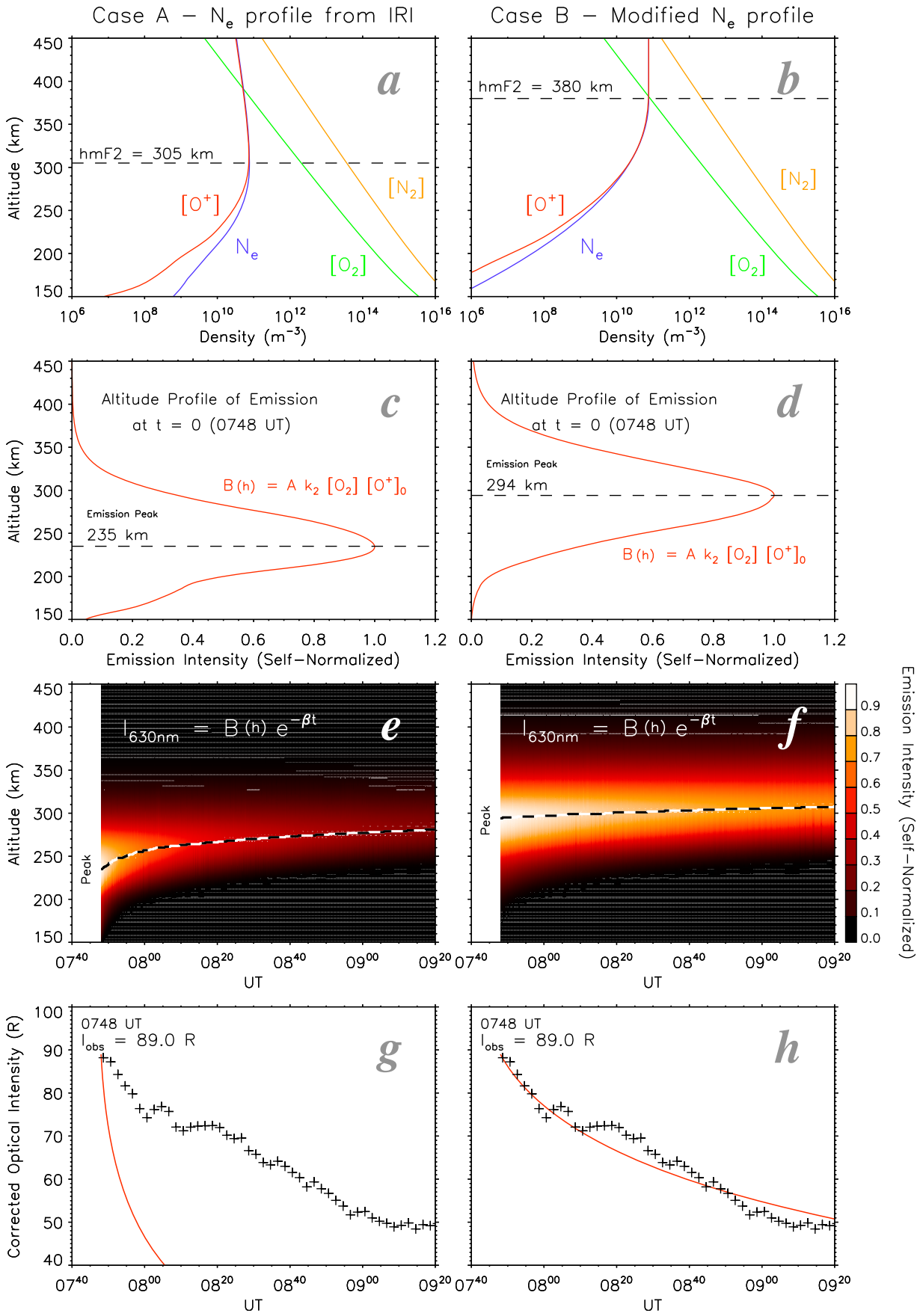
Case A – N_e profile from IRI
Case B – Modified N_e profile
a
b
hmF2 = 305 km
hmF2 = 380 km
$[O^+]$
N_e
$[N_2]$
$[O_2]$
Altitude (km)
Density (m^{-3})
c
d
Altitude Profile of Emission
at t = 0 (0748 UT)
Emission Peak
235 km
294 km
$B(h) = A\ k_2\ [O_2]\ [O^+]_0$
Emission Intensity (Self–Normalized)
e
f
$I_{630nm} = B(h)\ e^{-\beta t}$
Peak
UT
Emission Intensity (Self–Normalized)
g
h
0748 UT
I_{obs} = 89.0 R
Corrected Optical Intensity (R)

Figure 5

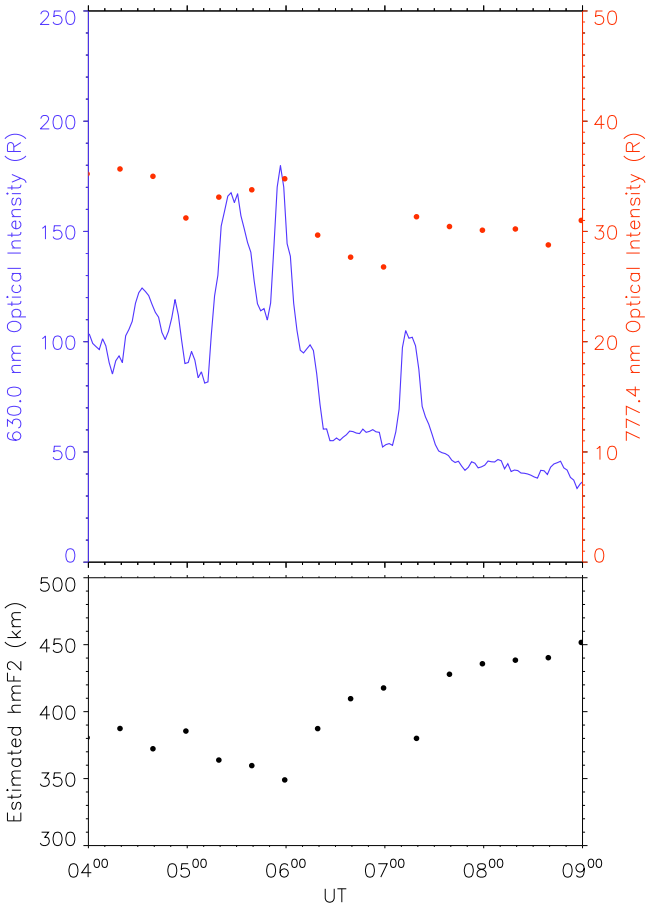

Figure 6. (top) Time series of the 630.0 nm (blue) and 777.4 nm (red) emissions at the zenith between 0400 and 0900 UT. Note that the 777.4 nm emission was sampled every 20 min. (bottom) Estimated h_mF_2 from the time series of the 630.0 and 777.4 nm emissions by using the equation of *Makela et al.* [2001].

Here, $I_{777.4}$ and $I_{630.0}$ is the emission intensity at the 630.0 nm and 777.4 nm wavelength in Rayleigh, respectively. Figure 6 (bottom) shows h_mF_2 estimated from the time series of the 630.0 nm and 777.4 nm emissions by using equation (14). At around 0718 UT, during the passage of patch F at zenith, the estimated peak height was around 380 km. This supports our speculation that the discrepancy shown in Figure 5g is primarily due to the wrong assumption of the F region peak height.

[10] Now, we turn to modify the altitude profile employed in the previous modeling by using the value of the F region peak height of 380 km which is estimated from comparison between 630.0 nm and 777.4 nm emissions. The electron density profile N_e (h) below the $F2$ region peak density in the IRI model is described by the following expression [*Ramanamurty and Rawer*, 1985]:

$$N_e = N_mF_2 \exp(-xB_1)/\cosh(x), x = (h_mF_2 - h)/B_0. \quad (15)$$

Here B_0 is the thickness parameter and B_1 is a shape parameter below the $F2$ region maximum. In order to improve the reproduction, we modify the IRI-based altitude profile of $[O^+]$ using equation (15). Figure 5b shows the modified profile of $[O^+]$, in which we employ the same N_mF_2, B_0 and B_1 as obtained from the IRI model while the height of the $F2$ region peak h_mF_2 is set to 380 km instead of 305 km. The ratio of O^+ to N_e is also obtained from the model. Thus, we only change the peak altitude of the F region according to the estimation from comparison between 630.0 nm and 777.4 nm emissions. We assume that the density is constant above h_mF_2 because the contribution to the observed optical intensity from the altitudes above h_mF_2 is not significant. Figure 5d shows the altitude profile of β calculated from the modified IRI profile shown in Figure 5b. The peak of the emission layer was at 294 km in altitude which is about 60 km higher than that calculated from the original IRI profile (Figure 5c). Figure 5f shows how the altitude profile of the optical intensity varied with time. The decay of the emission intensity becomes more gradual and the peak altitude did not change very much during the interval considered. This is due to lower reaction rates k_1 and k_2 in higher altitudes. The red curve in Figure 5h indicates the column emission intensity derived using equation (10). In contrast to Figure 5g, the reproduced optical intensity well explains the observed decay of patch luminosity. This good agreement suggests that the peak of the F region and 630.0 nm emission layer was located at higher altitude at around 380 km and 294 km, respectively, which allowed the patch to survive for more than 1 h.

[11] The decay of patch F can be quantitatively explained by the loss through recombinations of O^+ with ambient N_2 and O_2 molecules, if we assume the altitude of the optical patch to be around 295 km. In the recent studies of patches with the ASI at Resolute Bay [*Hosokawa et al.*, 2006, 2009a, 2009b, 2010a], we have assumed that the peak altitude of the 630.0 nm emission associated with patches was around 250 km, that is almost 50 km lower than the altitude of patch F estimated from the evaluation of its decay rate. As shown in Figure 4d, if we change the altitude of the patch, we get a quite different value of the loss rate. For example, β is $\approx 3 \times 10^{-4}$ s^{-1} at 250 km altitude and $\approx 7 \times 10^{-5}$ s^{-1} at 290 km altitude. These values of β give e-folding time of $\approx$ 1 h and 4 h, respectively. Such a drastic change of β with altitude is mainly because the densities of N_2 and O_2 decrease significantly with increasing altitude. It is well known that patches take a long time to travel from the dayside source region near the cusp toward the nightside auroral region. If we assume that the source of patch F was

Figure 5. (a) Altitude profile of the densities of electrons (blue), O^+ (red), N_2 (orange), and O_2 (green) obtained from the IRI and MSIS models (case A). (b) Same as Figure 5a, but h_mF_2 is set to 380 km (case B). (c, d) Altitude profile of the 630.0 nm emission at 0748 UT (t = 0) calculated from the O^+ profile for cases A and B, respectively. (e, f) Temporal evolution of the emission layer after 0748 UT for cases A and B, respectively. (g, h) Time series of the 630.0 nm optical intensity at the center of patch F after 0748 UT together with the reproduced variation of the patch luminosity.

located at 78° MLAT near 12 MLT and an average anti-sunward polar cap convection was 500 m s^{-1}, it could take more than 1 h for the patch to reach the FOV of the ASI at Resolute Bay (MLAT = 82.9°) near midnight. Thus, at the time of the arrival, the density in the lower-altitude part of the patch had decreased significantly through the long-lasting recombination process, while the density in the upper part probably remained high. This, in turn, implies that the central altitude of the patch increased as it traveled further toward the nightside across the dark polar cap. This could be one of the reasons why the altitude of patch F was estimated to be much higher than the nominal value. In this modeling, however, we ignore other factors which could affect the density profile of the patch, such as field-aligned plasma transport from the topside ionosphere and uplift of the ionosphere due to finite vertical component of E × B drift under the slightly oblique magnetic field at the polar cap latitudes. Thus, the above mentioned scenario is one of the possible explanations for the higher central altitude of patches in the nightside polar cap. *Lorentzen et al.* [2004] estimated the altitude of patches observed at Svalbard, Norway (MLAT ≈ 78°) near midnight using triangulation between two ground-based optical stations. During the events they investigated, the altitude of the optical patches was around 310–320 km. This is ≈ 20 km higher than the altitude of patch F over Resolute Bay (MLAT ≈ 83°. This again implies that the altitude of a patch increases as it travels further toward the nightside, which is consistent with *Moen et al.* [2008], who showed that h_mF_2 in the nightside polar cap was much higher than that derived from the IRI model. Namely, the current study points out that we should employ higher emission altitude probably around 300 km when we investigate patches detected by ground-based ASIs in the nightside polar cap. Such information is of particular importance when we compare the optical data with other instrument such as coherent radars [e.g., *Hosokawa et al.*, 2009a] by mapping the all-sky image on the geographic coordinate system with an assumption of the patch emission altitude.

[12] **Acknowledgments.** This work was supported by Grants-in-Aid for Scientific Research (16403007, 19403010, 20244080, and 20740282) from the Japan Society for the Promotion of Science (JSPS). This work was carried out by the joint research program of the Solar-Terrestrial Environment Laboratory (STEL), Nagoya University. The authors thank M. Satoh, Y. Katoh, H. Hamaguchi, and Y. Yamamoto of STEL, Nagoya University, for their helpful support in airglow imaging observations. Special thanks are extended to the staff of the Narwhal Arctic Service at Resolute Bay for kind and helpful support in operating the optical instrument. The optical observation at Resolute Bay was also supported by NSF cooperative agreement ATM-0608577. The authors wish to thank T. Nagai for access to data from MGF instruments onboard the Geotail spacecraft. This work was done while K.H. was staying at the Department of Physics, University of Oslo, as a guest researcher. His research at the University of Oslo was supported by an "Excellent Young Researcher Overseas Visit Program" grant from JSPS. J.M. has received support from the Norwegian Research Council, the Air Force Office of Scientific Research, Air Force Material Command, USAF, under grant FA8655-10-1-3003, and COST action ES0803.

[13] Robert Lysak thanks the reviewers for their assistance in evaluating this paper.

References

Bahcivan, H., R. Tsunoda, M. Nicolls, and C. Heinselman (2010), Initial ionospheric observations made by the new Resolute incoherent scatter radar and comparison to solar wind IMF, *Geophys. Res. Lett.*, *37*, L15103, doi:10.1029/2010GL043632.

Baker, K. B., and S. Wing (1989), A new magnetic coordinate system for conjugate studies of high latitudes, *J. Geophys. Res.*, *94*, 9139–9143.

Barbier, D. (1959), Recherches sur la raie 6300 de la luminescence atmosphrique nocturne, *Ann. Geofis.*, *15*, 179–217.

Barbier, D., and J. Glaume (1962), La couche ionospherique nocturne F dans la zone intertropicale et ses relations avec l'mission de la raie 6300 du ciel nocturne, *Planet. Space Sci.*, *9*, 133–148.

Bilitza, D., and B. Reinisch (2008), International Reference Ionosphere 2007: Improvements and new parameters, *Adv. Space Res.*, *42*, 599–609, doi:10.1016/j.asr.2007.07.048.

Coley, W. R., and R. A. Heelis (1995), Adaptive identification and characterization of polar ionization patches, *J. Geophys. Res.*, *10*, 23,819–23,827.

Cowley, S. W. H., and M. Lockwood (1992), Excitation and decay of solar wind-driven flows in the magnetosphere-ionosphere system, *Ann. Geophys.*, *10*, 103–115.

Crowley, G. (1996), Critical review of ionospheric patches and blobs, in *Review of Radio Science 1993–1996*, edited by W. R. Stone, pp. 619–649, Oxford Univ. Press, New York.

Hedin, A. E. (1991), Extension of the MSIS thermospheric model into the middle and lower atmosphere, *J. Geophys. Res.*, *96*, 1159–1172.

Hosokawa, K., K. Shiokawa, Y. Otsuka, A. Nakajima, T. Ogawa, and J. D. Kelly (2006), Estimating drift velocity of polar cap patches with all-sky airglow imager at Resolute Bay, Canada, *Geophys. Res. Lett.*, *33*, L15111, doi:10.1029/2006GL026916.

Hosokawa, K., K. Shiokawa, Y. Otsuka, T. Ogawa, J.-P. St-Maurice, G. J. Sofko, and D. A. Andre (2009a), The relationship between polar cap patches and field-aligned irregularities as observed with an all-sky airglow imager at Resolute Bay and the PolarDARN radar at Rankin Inlet, *J. Geophys. Res.*, *114*, A03306, doi:10.1029/2008JA013707.

Hosokawa, K., T. Kashimoto, S. Suzuki, K. Shiokawa, Y. Otsuka, and T. Ogawa (2009b), Motion of polar cap patches: A statistical study with all-sky airglow imager at Resolute Bay, Canada, *J. Geophys. Res.*, *114*, A04318, doi:10.1029/2008JA014020.

Hosokawa, K., T. Tsugawa, K. Shiokawa, T. Otsuka, T. Ogawa, and M. Hairston (2009c), Unusually elongated bright optical plume in the polar cap *F* region: Is it a tongue of ionization?, *Geophys. Res. Lett.*, *36*, L07103, doi:10.1029/2009GL037512.

Hosokawa, K., J.-P. St-Maurice, G. J. Sofko, K. Shiokawa, Y. Otsuka, and T. Ogawa (2010a), Reorganization of polar cap patches through shears in the background plasma convection, *J. Geophys. Res.*, *115*, A01303, doi:10.1029/2009JA014599.

Hosokawa, K., T. Tsugawa, K. Shiokawa, Y. Otsuka, N. Nishitani, T. Ogawa, and M. Hairston (2010b), Dynamic temporal evolution of polar cap tongue of ionization, *J. Geophys. Res.*, *115*, A12333, doi:10.1029/2010JA015848.

Hosokawa, K., J. I. Moen, K. Shiokawa, and Y. Otsuka (2011), Motion of polar cap arcs, *J. Geophys. Res.*, *116*, A01305, doi:10.1029/2010JA015906.

Jayachandran, P. T., K. Hosokawa, J. W. MacDougall, S. Mushini, R. B. Langley, and K. Shiokawa (2009), GPS total electron content variations associated with a polar cap arc, *J. Geophys. Res.*, *114*, A12304, doi:10.1029/2009JA014916.

Khan, H., and S. W. H. Cowley (1999), Observations of the response time of high-latitude ionospheric convection to variations in the interplanetary magnetic field using EISCAT and IMP-8 data, *Ann. Geophys.*, *17*, 1306–1335.

Koustov, A., K. Hosokawa, N. Nishitani, T. Ogawa, and K. Shiokawa (2008), Rankin Inlet PolarDARN radar observations of duskward moving Sun-aligned optical forms, *Ann. Geophys.*, *26*, 2711–2723.

Kubota, M., H. Fukunishi, and S. Okano (2001), Characteristics of medium- and large-scale TIDs over Japan derived from OI 630-nm nightglow observation, *Earth Planets Space*, *53*, 741–751.

Lockwood, M., and H. C. Carlson Jr. (1992), Production of polar cap electron density patches by transient magnetopause reconnection, *Geophys. Res. Lett.*, *19*, 1731–1734.

Lockwood, M., J. Moen, S. W. H. Cowley, A. D. Farmer, U. P. Løvhaug, H. Lühr, and V. N. Davda (1993), Variability of dayside convection and motions of the cusp/cleft aurora, *Geophys. Res. Lett.*, *20*, 1011–1014.

Lorentzen, D. A., N. Shumilov, and J. Moen (2004), Drifting airglow patches in relation to tail reconnection, *Geophys. Res. Lett.*, *31*, L02806, doi:10.1029/2003GL017785.

MacDougall, J. W., and P. T. Jayachandran (2007), Polar patches: Auroral zone precipitation effects, *J. Geophys. Res.*, *112*, A05312, doi:10.1029/2006JA011930.

Makela, J., M. Kelley, S. Gonzalez, N. Aponte, and R. McCoy (2001), Ionospheric topography maps using multiple-wavelength all-sky images, *J. Geophys. Res.*, *106*, 29,161–29,174.

McFarland, M., D. L. Albritton, F. C. Fehsenfeld, E. E. Ferguson, and A. L. Schmeltekopf (1973), Flow-drift technique for ion mobility and ion-molecule reaction rate constant measurements: 2. Positive ion reactions of N^+, O^+, and N_2^+ with O_2 and O^+ with N_2 from thermal to ≈ 2 eV, *J. Chem. Phys.*, *59*, 6620–6628.

Milan, S. E., M. Lester, and T. K. Yeoman (2002), HF radar polar patch formation revisited: Summer and winter variations in dayside plasma structuring, *Ann. Geophys.*, *20*, 487–499.

Moen, J., P. E. Sandholt, M. Lockwood, W. F. Denig, U. P. Løvhaug, B. Lybekk, A. Egeland, D. Opsvik, and E. Friis-Christensen (1995), Events of enhanced convection and related dayside auroral activity, *J. Geophys. Res.*, *100*, 23,917–23,934.

Moen, J., M. Lockwood, P. E. Sandholt, U. P. Løvhaug, W. F. Denig, A. Egeland, and A. P. van Eyken (1996), Variability of dayside high latitude convection associated with a sequence of auroral transients, *J. Atmos. Terr. Phys.*, *58*, 85–96.

Moen, J., H. C. Carlson, and P. E. Sandholt (1999), Continuous observation of cusp auroral dynamics in response to an IMF B_Y polarity change, *Geophys. Res. Lett.*, *26*, 1243–1246.

Moen, J., H. C. Carlson, K. Oksavik, C. P. Nielsen, S. E. Pryse, H. R. Middleton, I. W. McCrea, and P. Gallop (2006), EISCAT observations of plasma patches at sub-auroral cusp latitudes, *Ann. Geophys.*, *24*, 2363–2374.

Moen, J., N. Gulbrandsen, D. A. Lorentzen, and H. C. Carlson (2007), On the MLT distribution of *F* region polar cap patches at night, *Geophys. Res. Lett.*, *34*, L14113, doi:10.1029/2007GL029632.

Moen, J., X. C. Qiu, H. C. Carlson, R. Fujii, and I. W. McCrea (2008), On the diurnal variability in F2-region plasma density above the EISCAT Svalbard radar, *Ann. Geophys.*, *26*, 2427–2433.

Pedersen, T., B. Fejer, R. Doe, and E. Weber (1998), Incoherent scatter radar observations of horizontal *F* region plasma structure over Sondrestrom, Greenland, during polar cap patch events, *Radio Sci.*, *33*, 1847–1866.

Pedersen, T., B. Fejer, R. Doe, and E. Weber (2000), An incoherent scatter radar technique for determining two-dimensional horizontal ionization structure in polar cap *F* region patches, *J. Geophys. Res.*, *105*, 10,637–10,655.

Ramanamurty, Y. V., and K. Rawer (1985), Electron density reference profile in the lower ionosphere, *Adv. Space Res.*, *5*, 29–34.

Rodger, A. S., M. Pinnock, J. R. Dudeney, K. B. Baker, and R. A. Greenwald (1994), A new mechanism for polar patch formation, *J. Geophys. Res.*, *99*, 6425–6436.

Schunk, R., W. Raitt, and P. Banks (1975), Effect of electric fields on the daytime high-latitude *E* and *F* regions, *J. Geophys. Res.*, *80*, 3121–3130.

Shiokawa, K., Y. Katoh, M. Satoh, M. K. Ejiri, T. Ogawa, T. Nakamura, T. Tsuda, and R. H. Wiens(1999), Development of optical mesosphere thermosphere imagers (OMTI), *Earth Planets Space*, *51*, 887–896.

Shiokawa, K., Y. Katoh, M. Satoh, M. K. Ejiri, and T. Ogawa (2000), Integrating-sphere calibration of all-sky cameras for nightglow measurements, *Adv. Space Res.*, *26*, 1025–1028.

Shiokawa, K., Y. Otsuka, and T. Ogawa (2009), Propagation characteristics of nighttime mesospheric and thermospheric waves observed by optical mesosphere thermosphere imagers at middle and low latitudes, *Earth Planets Space*, *61*, 479–491.

Sojka, J. I., R. W. Schunk, M. D. Bowline, and D. J. Crain (1997), Ambiguity in identification of polar cap F-region patches: Contrasting radio and optical observation techniques, *J. Atmos. Sol. Terr. Phys.*, *59*, 249–258.

Suzuki, S., K. Shiokawa, K. Hosokawa, K. Nakamura, and W. K. Hocking (2009), Statistical characteristics of polar cap mesospheric gravity waves observed by an all-sky airglow imager at Resolute Bay, Canada, *J. Geophys. Res.*, *114*, A01311, doi:10.1029/2008JA013652.

Tohmatsu, T., and T. Ogawa (1990), *Compendium of Aeronomy*, Terra Sci., Tokyo.

Valladares, C., S. Basu, J. Buchau, and E. Friis-Christensen (1994a), Experimental evidence for the formation and entry of patches into the polar cap, *Radio Sci.*, *29*, 167–194.

Valladares, C., H. Carlson Jr., and K. Fukui (1994b), Interplanetary magnetic field dependency of stable Sun-aligned polar cap arcs, *J. Geophys. Res.*, *99*, 6247–6272.

Weber, E. J., J. Buchau, J. G. Moore, J. R. Sharber, R. C. Livingston, J. D. Winningham, and B. W. Reinisch (1984), *F* layer ionization patches in the polar caps, *J. Geophys. Res.*, *89*, 1683–1694.

K. Hosokawa, Department of Communication Engineering and Informatics, University of Electro-Communications, Chofugaoka 1-5-1, Chofu, Tokyo 182-8585, Japan. (hosokawa@ice.uec.ac.jp)

J. I. Moen, Department of Physics, University of Oslo, P. O. Box 1048, N-0316 Blindern, Norway. (j.i.moen@fys.uio.no)

Y. Otsuka and K. Shiokawa, Solar-Terrestrial Environment Laboratory, Nagoya University, Furo-cho, Chikusa-ku, Nagoya 464-8601, Japan. (otsuka@stelab.nagoya-u.ac.jp; shiokawa@stelab.nagoya-u.ac.jp)